Supporting Information

Electrocatalytic oxygen evolution activity of nickel-doped manganese oxide nanorods in acid

Bowen Xin, Yvpei Li, Dong Wang, Peize Xing, Chao Wang*

Department of Chemistry and Chemical Engineering, The Youth Innovation Team of Shaanxi Universities, Shaanxi University of Science and Technology, Xi'an, Shaanxi 710021, China

* Corresponding author:

cwang@sust.edu.cn

1. Experimental
2. Instrumentation
3. X-ray photoelectron spectroscopy
4. X-ray diffraction
5. EDS and ICP-AES
6. Electrochemistry
7. Activity comparison
8. TEM
9. References

1. Experimental

Chemicals

$K_2S_2O_8$ (Hongyan Chemical Reagent; AR 99.5%), Manganous sulfate monohydrate, ($MnSO_4 \cdot H_2O$; Damao Chemical Reagent; AR 99.0%), Nickel nitrate hexahydrate ($Ni(NO_3)_2 \cdot 6H_2O$; Kemiou Chemical Reagent; AR 99.0%), ethanol absolute (Guanghua Chemical Reagent; AR 99.7%), Potassium sulphate (K_2SO_4;Guanghua Chemical Reagent; AR 25-28%), carbon paper were used as received unless stated otherwise. Doubly distilled water was used throughout the experiment.

2. Instrumentation

X-ray photoelectron spectroscopy (XPS) was carried out using a Kratos Axis Supra spectrometer at room temperature and ultra-high vacuum (UHV) conditions. The instrument was equipped with monochromatic Al Kα source 1486.6 eV (15 mA, 15 kV), and hemispherical analyser with hybrid magnetic and electrostatic lens for enhanced electron collection. Survey and detailed XPS spectra were acquired at normal emission with the fixed pass energy of 160 eV and 40 eV, respectively. All spectra were charge-corrected to the hydrocarbon peak set to 284.6 eV. The Kratos charge neutralizer system was used on all specimens. Data analysis was based on a standard deconvolution method using mixed Gaussian (G) and Lorentzian (L) line shape (G = 70% and L = 30%, Gaussian–Lorentzian product) for each component. Spectra were analyzed using CasaXPS software (version 2.3.16). X-ray diffraction (XRD) was acquired using (D8 ADV ANCE, Bruker) diffractometer having Cu Kα (λ=1.54 Å) source. The instrument was operated at 30 mA current voltage and 40 kV. Field emission scanning electron microscope (S-4800, Hitachi, Japan) and transmission electron microscope (FEI-Tecnai G2 F20) were used to observe the morphology of the catalyst. ICP-AES parameters are the following: forward power 1350 W, plasma gas flow rate 12.0 L min^{-1}, nebulizer gas flow rate 1.0 L min^{-1}, auxiliary gas flow rate 1.0 L min^{-1}, sample uptake speed 50 rpm with white/orange Tygon tubing. A concentric nebulizer was used with a cyclonic spray chamber. No internal standard correction was applied for ICP-AES analysis.

3. X-ray photoelectron spectroscopy

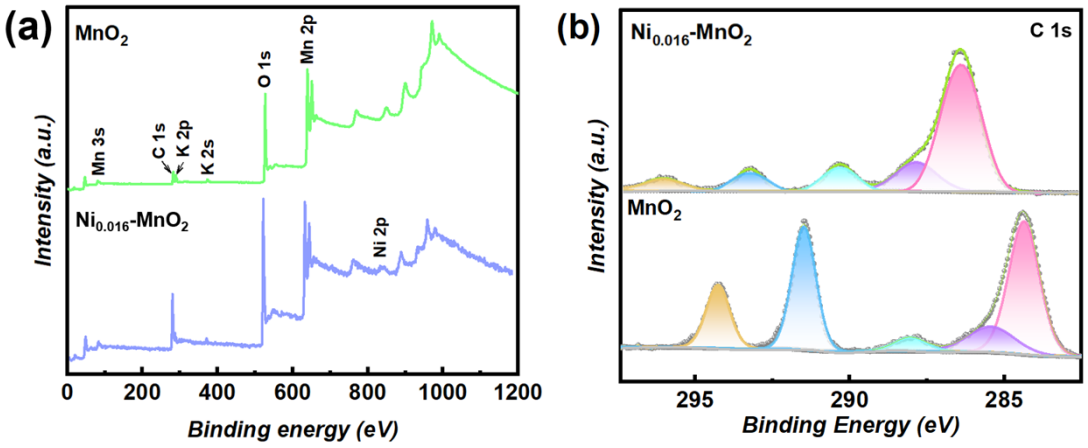

Figure S1. (a) XPS survey spectra of the $Ni_{0.016}$-MnO_2 and MnO_2; (b) Deconvoluted high-resolution XPS spectra of the C 1s region of $Ni_{0.016}$-MnO_2 and MnO_2.

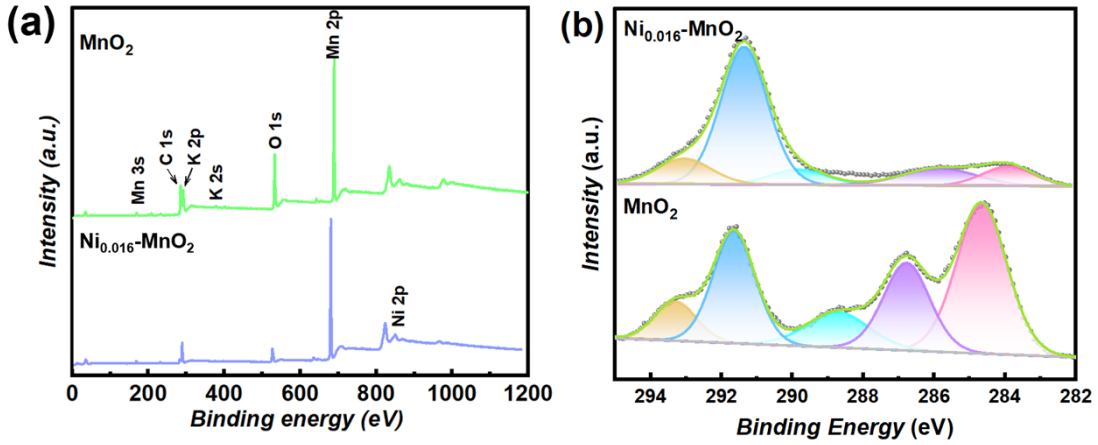

Figure S2. (a) XPS survey spectra of the $Ni_{0.016}$-MnO_2 and MnO_2/CP after the long-term galvanostatic test; (b) Deconvoluted high-resolution XPS spectra of the C 1s region of $Ni_{0.016}$-MnO_2 and MnO_2/CP after the long-term galvanostatic test.

4. X-ray diffraction

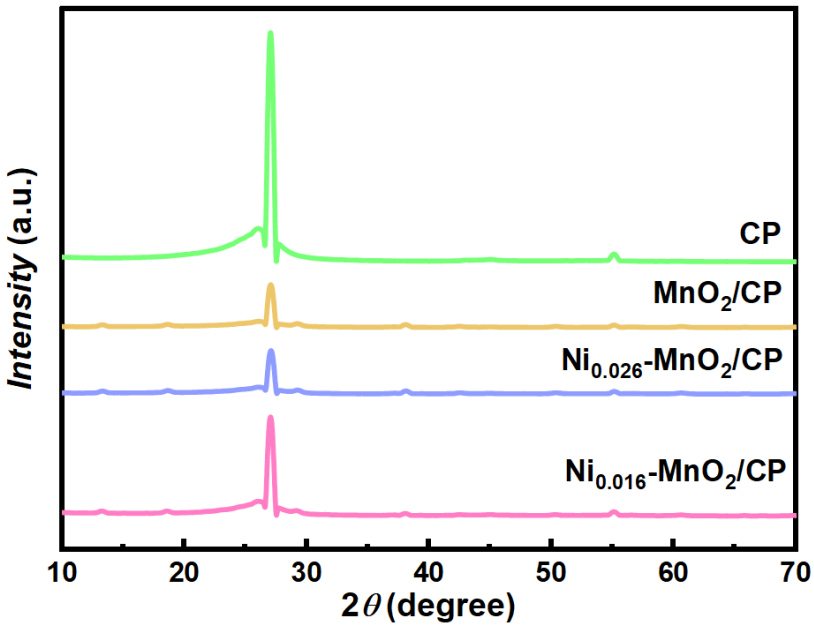

Figure S3. XRD patterns of the $Ni_{0.016}$-MnO_2, $Ni_{0.026}$-MnO_2, MnO_2/CP and a bare CP after long-term galvanostatic test.

5. EDS and ICP-AES

Table S1. Content of the elements in the sample by ICP-AES

	Atomic Percentage (%)	
	Ni	Mn
$Ni_{0.016}$-MnO_2	1.65	98.35
$Ni_{0.026}$-MnO_2	2.61	97.39

Table S2. The amount of elements dissolved into the electrolytes after long-term OER

ICP-AES		Ni	Mn
Dissolved mass (mg)	MnO_2	-	0.617
	$Ni_{0.016}$-MnO_2	0.003	0.625
	$Ni_{0.026}$-MnO_2	0.483	0.296
Atomic Percentage(%)	MnO_2	-	20.57
	$Ni_{0.016}$-MnO_2	0.001	20.83
	$Ni_{0.026}$-MnO_2	0.161	0.099

Table S3. The content of different oxygen groups by XPS

XPS		Atomic Percentage (%)		
		-O	-OH	$-H_2O$
Before	MnO_2	32.44	46.23	21.33
	$Ni_{0.016}$-MnO_2	46.81	44.32	8.87
After	MnO_2	97.35	1.76	0.89
	$Ni_{0.016}$-MnO_2	61.48	32.81	5.71

6. Electrochemistry

The conversion from the measured SCE scale to the RHE scale is based on equ. S1.

$$E_{RHE} = E_{SCE} + 0.241 + 0.059\ pH. \quad (S1)$$

where, E_{RHE} is the potential energy at the RHE scale, and E_{SCE} is the potential obtained vs. SCE. The EIS is measured in the frequency range of 0.1 - 10^{-5} Hz with an alternating voltage amplitude of 5 mV. Solution resistance (R_s) values obtained from the EIS are used for *iR* compensation, and LSV and *E-t* curves are *iR* compensated (Table S4) calculated by eqn. S2.

$$E_{iR\text{-corrected}} = E - iR \quad (S2)$$

The Tafel slope (b) is calculated by eqn. S3.

$$\eta = b \log j \quad (S3)$$

The η of OER is calculated by eqn. S4.

$$\eta = E_{RHE} - 1.229 \quad (S4)$$

The double layer capacitance (C_{dl}) was measured using CV at various scan rates in the non-Faradaic region, and was estimated by plotting $\Delta i = i_a - i_c$ (where i_a and i_c are anodic and cathodic current, respectively) against the scan rate. The slope yields $2C_{dl}$. The electrochemical active surface area (EASA) is calculated based on eqn. S5,

$$EASA = C_{dl} / C_s \quad (S5)$$

where C_s is the conversion factor of 0.015 mF cm^{-2}.

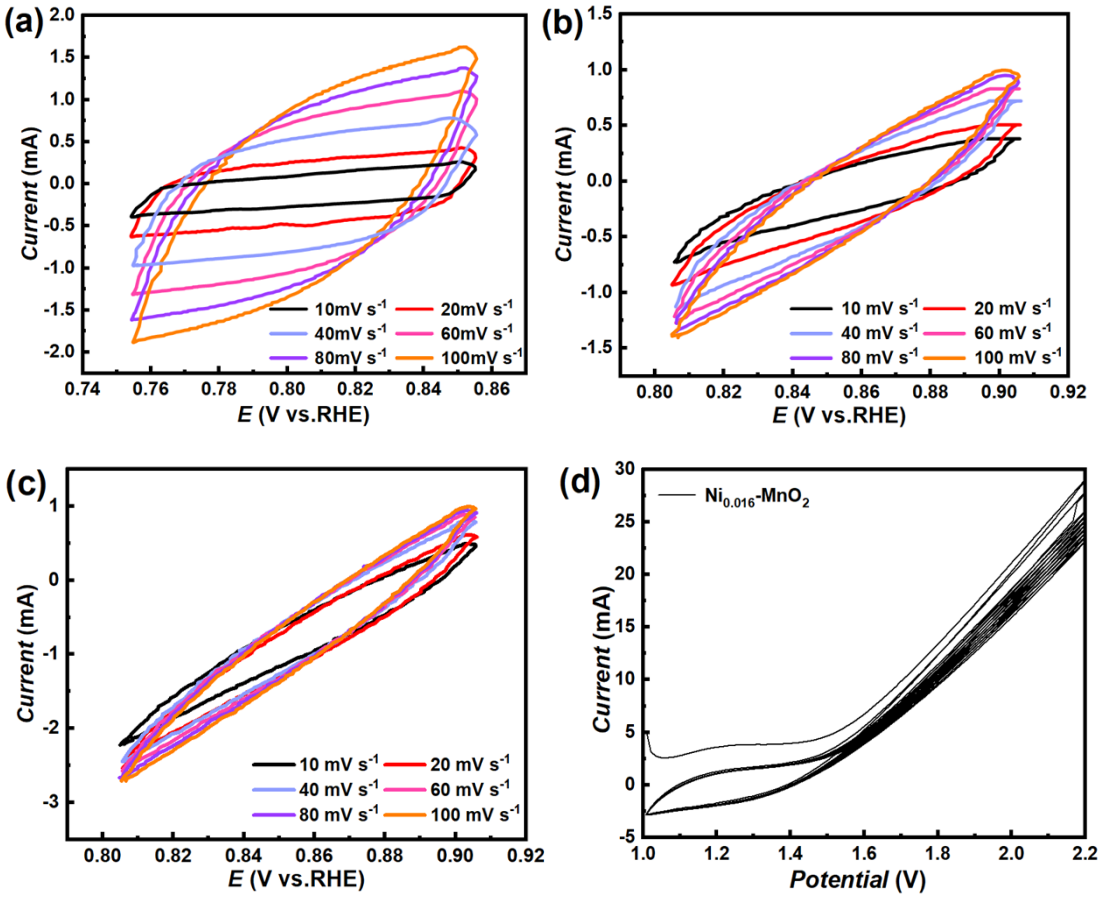

Figure S4. (a-c) CV of $Ni_{0.016}$-MnO_2, $Ni_{0.026}$-MnO_2, and MnO_2/CP at different scan rates (10,20, 40, 60, 80, and 100 mV s^{-1}) in 1 M $HClO_4$. (d) Initial 10 cycle CV of $Ni_{0.016}$-MnO_2/CP at 5 mV s^{-1} in 0.1 M $HClO_4$.

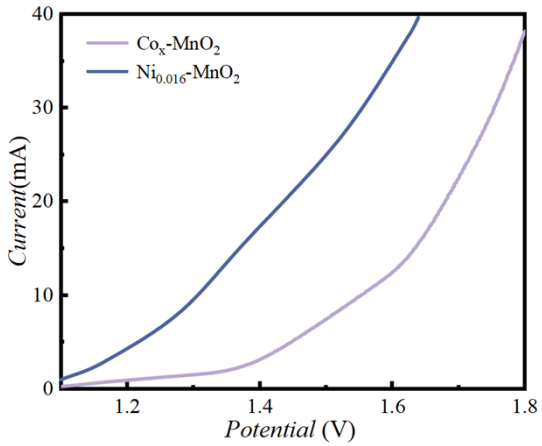

Figure S5. LSV of $Ni_{0.016}$-MnO_2/CP and Co_x-MnO_2/CP at 5 mV s^{-1} in 0.1 M $HClO_4$.

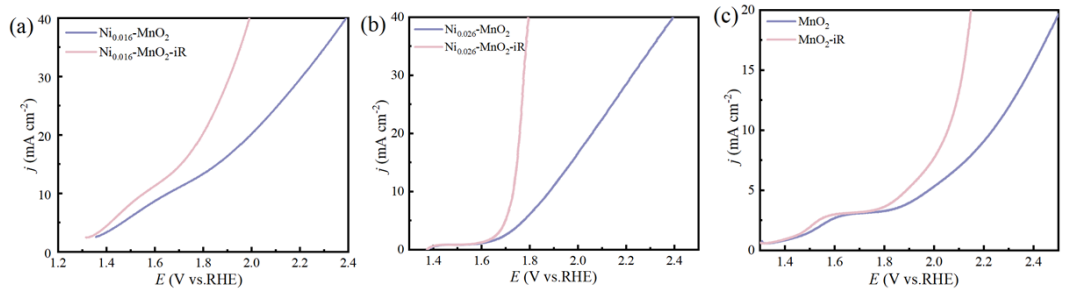

Figure S6. Comparison of the LSV curves with or without *iR*-compensation.

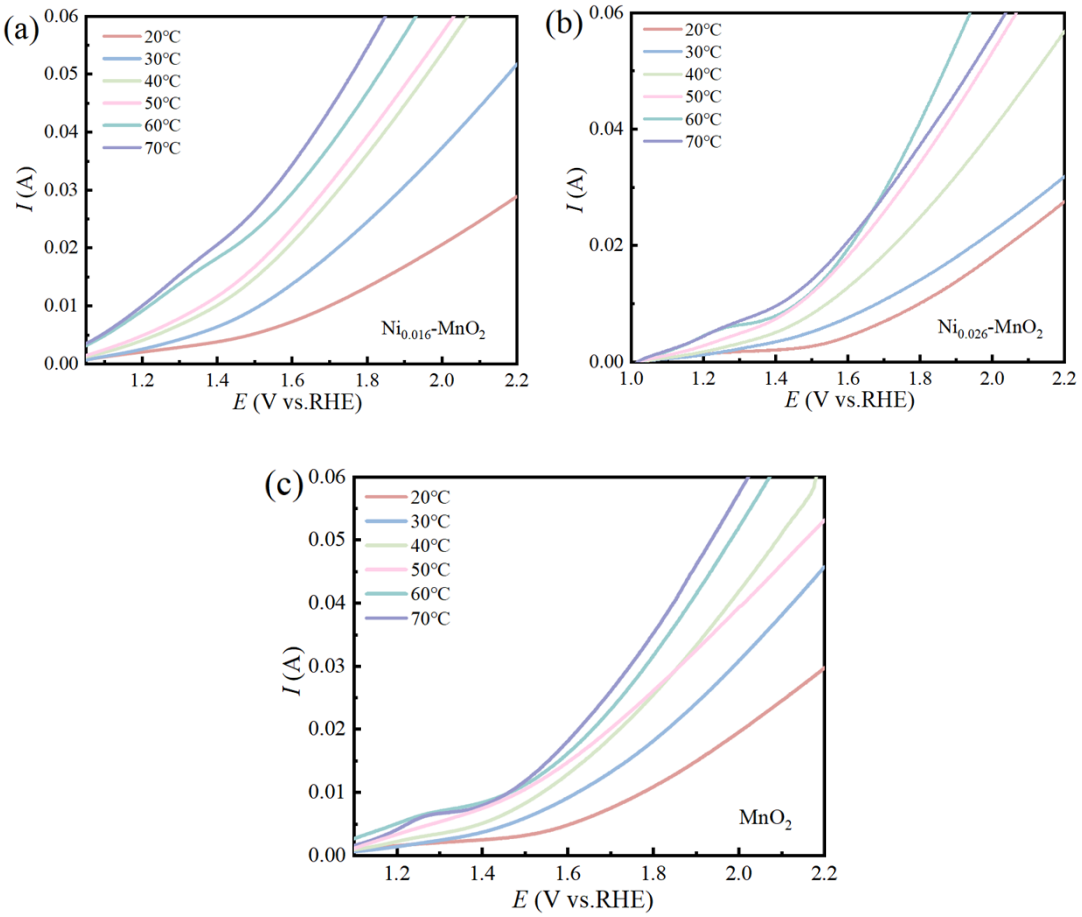

Figure S7. (a-c) LSV of $Ni_{0.016}$-MnO_2/CP, $Ni_{0.026}$-MnO_2/CP and MnO_2/CP at different temperature at 5 mV s^{-1} in 0.1 M $HClO_4$.

The pH dependence of the OER rate is analyzed in this manuscript. We arbitrarily selected different potentials in the RHE scale (equivalent to the overpotential) in the OER region, and calculate the m_{H+} by eqn. S6.

$$m_{H+} = \left(\frac{\partial log j}{\partial log[H^+]}\right)_\eta \qquad \text{(S6)}$$

The OER happens through different mechanistic pathways. The adsorbate evolution mechanism (AEM) involve four proton-coupled electron transfer steps (eqn. S7-S10).

$$M + H_2O \rightarrow M\text{-}OH + H^+ + e^- \qquad \text{(S7)}$$

$$M\text{-}OH \rightarrow M\text{-}O + H^+ + e^- \qquad \text{(S8)}$$

$$M\text{-}O + H_2O \rightarrow M\text{-}OOH + H^+ + e^- \qquad \text{(S9)}$$

$$M\text{-}OOH \rightarrow M + H^+ + e^- + O_2 \qquad \text{(S10)}$$

If OER proceeds through the AEM, zero dependence on the pH should be observed in the RHE scale. Other mechanistic pathway is also possible, for example, the lattice oxygen oxidation mechanism (LOM), where a chemically proton transfer proceeds electron transfer process (Eq. S11-S12).

$$M\text{-}OH \rightarrow M\text{-}O^- + H^+ \qquad \text{(S11}$$

$$M\text{-}O^- \rightarrow M\text{-}O + e^- \qquad \text{(S12)}$$

In this case, the proton-transfer and electron transfer are decoupled, and the OER rate is dependent on the pH, and the m_{H+} is non-zero. For all the Ni_x-MnO_2/CP, the m_{H+} is not zero, which indicates that the decoupled proton and electron transfers are involved.

Theoretically, a simple electrochemical redox reaction can be described by the Butler-Volmer equation:

$$j = j_0\{\exp(-\alpha f\eta) - \exp[(1-\alpha) f\eta]\} \quad (6)$$

By taking logarithm of Eq. 1, and assuming the reverse reaction negligible, there is

$$\log j = \log j_0 + \alpha f\eta/2.303RT \quad (7)$$

where α is the transfer coefficient, f denotes F/RT (F: the Faraday's constant, R: the universal gas constant, T: the absolute temperature), and j_0 is the exchange current density. Therefore, by plotting the log j vs. η plot, the j_0 can be acquired from the intercept.

The j_0 of MOR for MnO_2 , $Ni_{0.016}$-MnO_2 and $Ni_{0.026}$-MnO_2/CP are 3.71 × 10^{-3} mA cm^{-2}, 8.85 × 10^{-4} mA cm^{-2} and 1.67 × 10^{-3} mA cm^{-2}, respectively.

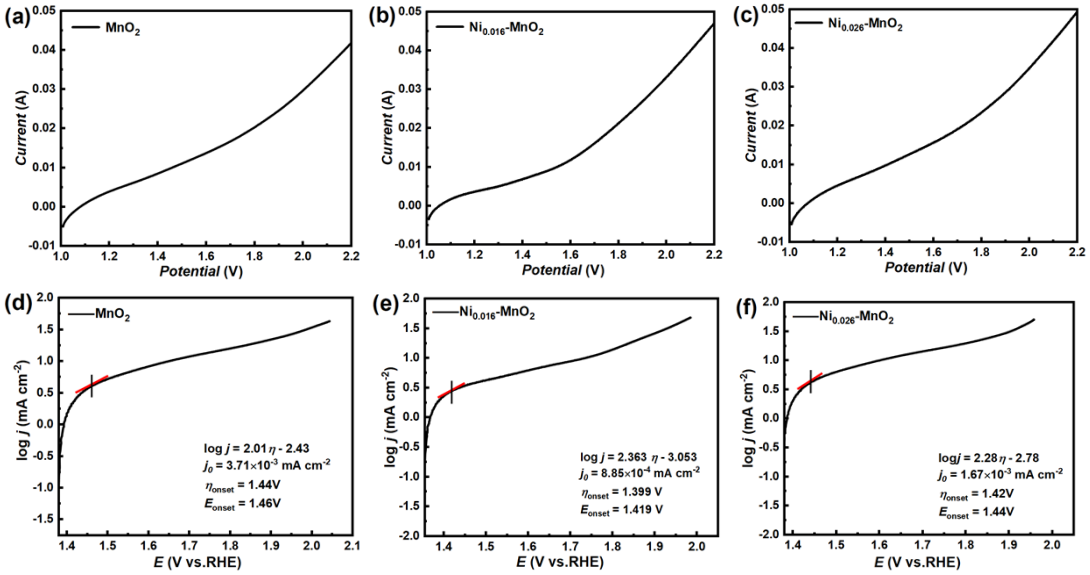

Figure S8. The LSV of the MnO_2 , $Ni_{0.016}$-MnO_2 and $Ni_{0.026}$-MnO_2/CP electrodes in 0.5 M CH_3OH + 1 M $HClO_4$ (scan rate 5 mV s^{-1}).

Table S4. EIS fitting results

	R_S/Ω	*Error*/%	R_{CT}/Ω	*Error*/%
$Ni_{0.016}$-MnO_2	12.43	0.289	40.66	0.854
$Ni_{0.026}$-MnO_2	15.91	0.556	60.73	3.037
MnO_2	17.52	0.479	215.81	3.502

7. Activity comparison

Table S5. OER activity comparison in acid

Catalysts	Electrolyte	η@10 mA cm^{-2}/mV	Tafel Slope/ mV dec^{-1}	Stability/h	References
$Ni_{0.016}$-MnO_2/CP	0.1 M $HClO_4$	390	61.66	5.5	This work
$NiMn_{1.5}Co_3O_{4-\delta}$	0.5 M H_2SO_4	280	108	80	[1]
NiFeP	0.05 M H_2SO_4	540	60	30	[2]
$Ni_{0.5}Mn_{0.5}Sb_{1.7}O_y$	1.0 M H_2SO_4	670	60	168	[3]
γ-MnO_2	1.0 M $HClO_4$	490	80	8000	[4]
$Cu_{1.5}Mn_{1.5}O_4$:10F	0.5 M H_2SO_4	325	60	24	[5]
$RuO_2(Co,Mn)_3O_4$/CC	0.5 M H_2SO_4	270	77	24	[6]
Ti-MnO_2	0.05 M H_2SO_4	500	170	2	[7]
AlNiCoIrMo	0.5 M H_2SO_4	233	55.2	-	[8]
PMFCP	0.5 M H_2SO_4	390	472	8.3	[9]

8. TEM

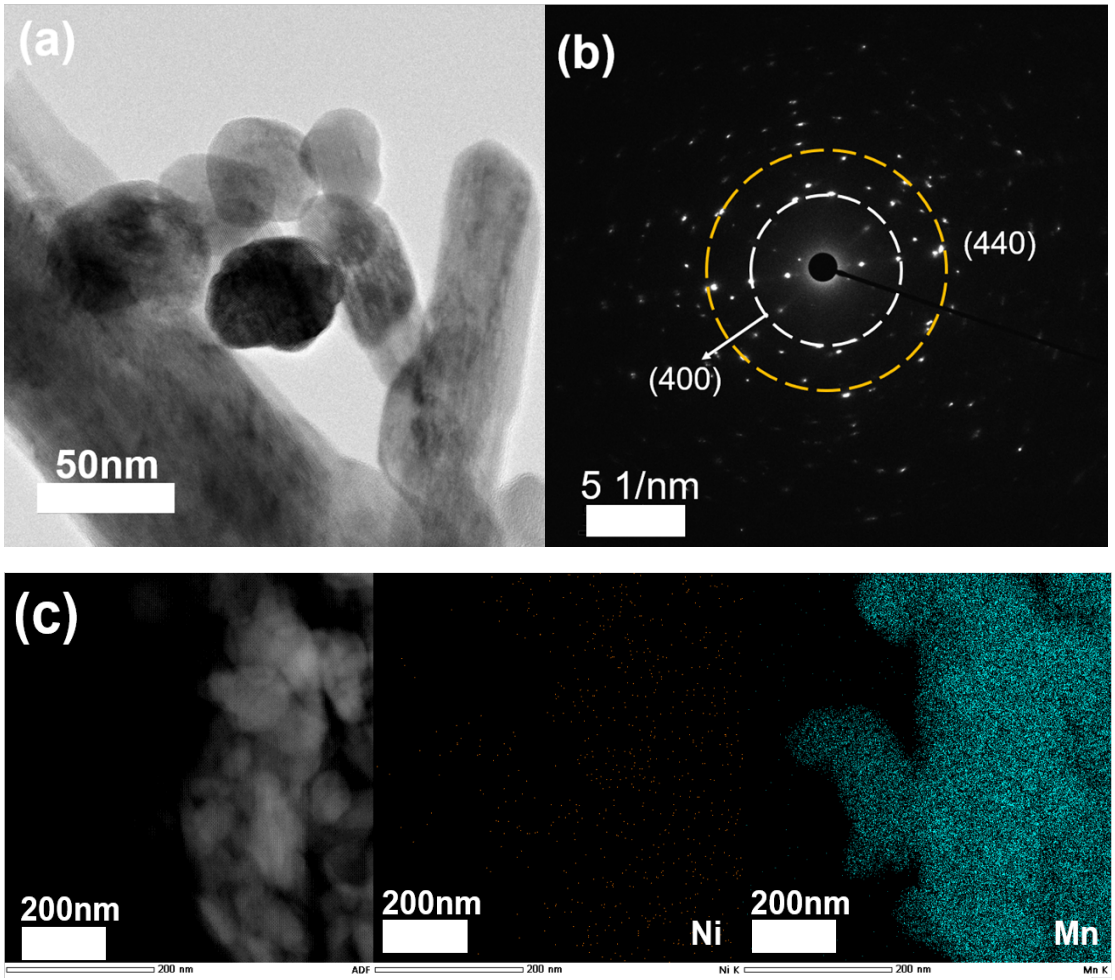

Figure S9. (a) TEM image of the $Ni_{0.016}$-MnO_2; (b) SAED pattern of the $Ni_{0.016}$-MnO_2; (d) Elemental mapping and HAADF image of the $Ni_{0.016}$-MnO_2

9. References

[1] Hongyu Zhao, Liu Zhu, Jie Yin, Jing Jin, Xin Du, Lei Tan, Yong Peng, Pinxian Xi, Chun-Hua Yan First published: 17 March 2024

[2] F. Hu, S. Zhu, S. Chen, Y. Li, L. Ma, T. Wu, Y. Zhang, C. Wang, C. Liu, X. Yang, L.

Song, X. Yang, Y. Xiong, Adv. Mater. 2017, 29, 1606570.

[3] I. A. Moreno-Hernandez, C. A. MacFarland, C. G. Read, K. M. Papadantonakis, B. S. Brunschwig, N. S. Lewis, Energy Environ. Sci. 2017, 10, 2103

[4] A. Li, H. Ooka, N. Bonnet, T. Hayashi, Y. Sun, Q. Jiang, C. Li, H. Han, R. Nakamura, Angew. Chem. Int. Ed. 2019, 58, 5054.

[5] P. P. Patel, M. K. Datta, O. I. Velikokhatnyi, R. Kuruba, K. Damodaran, P. Jampani, B. Gattu, P. M. S10 Shanthi, S. S. Damle, P. N. Kumta, Sci. Rep. 2016, 6, 28367.

[6] KUMAR R S, KARTHIKEYAN S, RAMAKRISHNAN S, et al. Anion dependency of spinel type cobalt catalysts for efficient overall water splitting in an acid medium [J]. Chemical Engineering Journal, 2023, 451: 138471

[7] R. Frydendal, E. A. Paoli, I. Chorkendorff, J. Rossmeisl, I. E. L. Stephens, Adv. Energy Mater. 2015, 5, 1500991.

[8] SU H, ZHAO X, CHENG W, et al. Hetero-N-coordinated Co single sites with high turnover frequency for efficient electrocatalytic oxygen evolution in an acidic medium [J]. ACS Energy Letters, 2019, 4(8): 1816-22.

[9] H. Liu, X. Peng, X. Liu, G. Qi, J. Luo, ChemSusChem 2019, 12, 1334.